Energy 166 (2019) 471–489

Contents lists available at ScienceDirect

Energy

journal homepage: www.elsevier.com/locate/energy

Investigation of wake characteristics for the offshore floating vertical axis wind turbines in pitch and surge motions of platforms

Hang Lei [a], Jie Su [a], Yan Bao [a], Yaoran Chen [a], Zhaolong Han [a, b, *], Dai Zhou [a, b, c, d, **]

[a] School of Naval Architecture, Ocean & Civil Engineering, Shanghai Jiao Tong University, Shanghai, 200240, PR China
[b] Collaborative Innovation Center for Advanced Ship and Deep-Sea Exploration (CISSE), Shanghai, 200240, PR China
[c] State Key Laboratory of Ocean Engineering, Shanghai Jiao Tong University, Shanghai, 200240, PR China
[d] Key Laboratory of Hydrodynamics of Ministry of Education, Minhang Campus, Shanghai, 200240, PR China

ARTICLE INFO

Article history:
Received 27 June 2018
Received in revised form
18 September 2018
Accepted 16 October 2018
Available online 19 October 2018

Keywords:
Floating vertical axis wind turbines
Wake characteristics
Pitch motion
Surge motion
CFD method
IDDES

ABSTRACT

Pitch and surge motions of platforms are two main movements of offshore floating vertical axis wind turbines when they are faced with wind and wave loads. These two movements can not only affect the aerodynamic loads, but also may influence the wake characteristics of the wind turbines. In the present study, the computational fluid dynamics approach with the improved delayed detached eddy simulation (IDDES) and the overset mesh are employed to investigate the wake characteristics of an H-rotor floating vertical axis wind turbine under the platform's pitch and surge motions. The wake profiles and structures between pitch and non-pitch conditions, and surge and non-surge conditions are compared. Then, the wake characteristics under different pitching amplitudes and periods and different surging amplitudes and periods are investigated. It is shown that pitch motion can enlarge the peak values of wake deficits and shift the positions of the mainstream of the wake in the vertical direction. The amplitudes and periods of the 'wake wave' under different pitching amplitudes and periods show regular variations. A 'Spindle' -type of wake structure is formed in the wake region under a platform's surge motion, and the strength and core zone of the 'Spindle' also regularly change with different surging amplitudes and periods. These changes cause wake profile's diversity at certain motion stages for the same downwind distance under different periods and amplitudes of surge and pitch.

1. Introduction

In recent years, wind turbines have been gradually developing into a large scale and moving towards the deep sea so as to get a higher wind energy conversion efficiency [1,2]. Large scale wind turbines can generate a larger wind power output due to the fact that doubling the rotor diameter can increase the power of the wind turbines by four times [3]. Higher quality wind resources with larger wind speed and lower turbulence intensity can be obtained in offshore environments [4]. The large scale wind turbines that are installed in offshore areas will not only generate a higher efficiency in wind energy conversion, but also pay well in economy [5,6]. Hence, the rapid development of deep-sea wind power technology is one of the most promising directions for future developments in the wind power industry. Nevertheless, many scientific and technical problems still exist in exploring the technology of the offshore floating wind turbines, such as aerodynamics, mooring line and structural dynamics, and hydrodynamics and coupled modeling approaches [7–9].

For aerodynamic problems, many studies have been conducted in the field of horizontal axis wind turbines (HAWTs) to investigate power performance, unsteady aerodynamic loads, wind farm layout and so on. For example, Sebastian and Lackner [10] utilized a reduced frequency analysis to investigate the aerodynamic performance of offshore floating HAWTs. Lin et al. [11] reported that the unsteady aerodynamic performance of the wind turbine rotor is profoundly affected by the platform motions and that the wake velocity became asymmetric and more complicated under the platforms' pitch and surge motions. Compared to HAWTs, there is relatively little research that focuses on the aerodynamic performance of floating vertical axis wind turbines (VAWTs). In recent

* Corresponding author. School of Naval Architecture, Ocean & Civil Engineering, Shanghai Jiao Tong University, Shanghai, 200240, PR China.;
** Corresponding author. School of Naval Architecture, Ocean & Civil Engineering, Shanghai Jiao Tong University, Shanghai, 200240, PR China.
E-mail addresses: han.arkey@sjtu.edu.cn (Z. Han), zhoudai@sjtu.edu.cn (D. Zhou).

https://doi.org/10.1016/j.energy.2018.10.101
0360-5442/

years, offshore floating VAWTs have been regarded as another promising wind turbine concept, which has many unique characteristics and can be treated as a complement to offshore floating HAWTs in the offshore wind turbine industry.

To better understand the aerodynamics of VAWTs, three main computational methods, including momentum theory, vortex theory, and computational fluid dynamics (CFD) theory, are used in analyzing the aerodynamic forces, power output, and wake characteristics in the past decades [12]. With the constant growth of computer technology and numerical approaches, the CFD method is attracting an increasing amount of favor because it can not only provide accurate calculation results, but also describe more detailed flow fields [13]. Elkhoury et al. [14] studies the aerodynamic performance of a variable-pitch VAWT by using the Large Eddy Simulation (LES) with a dynamic smagorinsky subgrid scale (SGS) model and wind tunnel test, indicating that the LES approach can precisely predict power coefficients at a wide range of tip speed ratios (TSRs). Buchner et al. [15] employed both the two-dimensional unsteady Reynolds-averaged Navier–Stokes (URANS) equations with the Menter-SST turbulence model and the wind tunnel test to investigate the dynamic stall of a VAWT, showing that the simulation results agreed well with experimental data. By comparing the results predicted by the three-dimensional URANS and Improved Delayed Detached Eddy Simulation (IDDES) with the experimental data, Lei et al. [16] reported that the power coefficient and wake velocity obtained by the IDDES are more accurate than those of the URANS, indicating that IDDES is a valuable tool for simulating the flow characteristics of vertical axial wind turbines.

Among the aerodynamic problems, the wake performance of VAWTs is quite important because it directly affects the spatial distribution of wind turbines in the wind farm [17]. The wake velocity behind the wind turbines is decreased as the wind kinetic-energy is converted into electric energy. The power output of the wind turbines decreases when the adjacent wind turbines are installed in the velocity-reduced region [18]. Besides, the turbulence intensity that is induced by the disturbance of the rotor's rotation in the wake region will increase and influence the aerodynamic loads on the blades of the wind turbine in the downstream region [19]. These effects will play a major role in the wind farm layout, which could affect the efficiency and durability of the entire wind farm significantly. Therefore, the wake study of VAWTs is very meaningful work. Based on these factors, many scholars have conducted some researches to study the wake characteristics of VAWTs by using both experimental and numerical methods [20]. Posa et al. [21] conducted a wind tunnel measurement associated with particle imaging velocimetry (PIV) and the LES approach to explore the wake structure of a VAWT. They found that stronger dynamic stall phenomena occurring at lower rotational speeds can cause higher asymmetry and larger vortices. In addition to the CFD method, a free vortex wake model was employed by Tescione et al. in analyzing the wake flow of a VAWT [22]. Comparing with the experiments, they reported that this model can capture all the important dynamics in the near wake of the rotor. Whereas, a quantitative analysis of the wake velocity was not demonstrated in detail in their study. To more clearly reflect the wake velocity distribution, Lam and Peng [23] reported that the wake characteristics predicted by three-dimensional CFD method were more accurate and detailed than those predicted by two-dimensional CFD simulations by comparing them with a PIV test. Shamsoddin and Porté-Agel [24] depicted the wake profiles of a VAWT in the Atmospheric Boundary Layer by using the LES framework associated with the actuator line model (ALM). The characteristics of wake turbulence were also demonstrated, which can act as the fundamental laws for the further wind farm optimizing. Moreover, a wind tunnel experiment was conducted to quantificationally analyze the wake characteristics for a H-rotor wind turbine [25]. Meanwhile, the LES method that can mutually verify the experimental results was also used to explain the mechanism for a fast wake recovery in the condition of grid turbulence. The self-similarity and flow characteristics of the wake for a VAWT were investigated by Abkar and Dabiri by using LES framework, and the self-similar properties of the wake velocity were found in their study [26].

All of these researches mentioned above focused on the wake characteristics of VAWTs just in the bottom-fixed condition. However, floating VAWTs must be faced with wind and wave loads and generated six-degree of freedom motions (6-DOF) under normal working conditions. The 6-DOF motion that leads to the change of aerodynamic performance has been investigated by the authors in previous studies [27,28]. According to the experience in studying HAWTs, the wake characteristics of the wind turbine also changed due to the 6-DOF motions of the platforms [29]. Many published literature investigated the impacts of 6-DOF motions of the platforms on the wake performance of HAWTs [10,30–33]. Nevertheless, there is still very little relative research concerning the wake structures of VAWTs in 6-DOF motion. Further, pitch and surge motions are the key movements of floating wind turbines under the joint action of wind and wave loads [34,35]. Understanding the wake characteristics of VAWTs under the motions of the platforms is the first step to developing the appropriate wake model. It must be the crucial factor for the optimization of offshore vertical axis wind farms. In addition, understanding the wake characteristics of wind turbines in surge motion and pitch motion respectively can effectively guide the platform design. Because each of the 6-DOF motions has its unique additional movement among the whole movements of the floating wind turbines, thus the wake variations for the wind turbine in a certain motion have the special features. In the platform design phase, designer can control the certain motions of the platforms according to hydrodynamic knowledge.

The purpose of this paper is to investigate the wake characteristics of an H-rotor wind turbine in platform's pitch and surge motions. To achieve this objective, the CFD method with the IDDES model and the overset mesh technique are employed. The available experimental data from others' research is used to verify the reliability of the present CFD model. The simulation results, including the comparisons of wake profiles between motion and non-motion conditions, wake profiles and structures under different pitching periods and amplitudes, and wake profiles and structures under different surging periods and amplitudes, will be demonstrated and discussed in detail.

2. Wind turbine geometry model

Offshore floating VAWTs are just in the conceptual design phase, and thus they have not been used in commercial projects yet. Therefore, experimental data for full size offshore floating VAWTs is still unavailable. To overcome this difficulty and obtain the available experimental data, a reduced scale VAWT model which comes from Mie university is utilized in the present study [36]. The reasons for adopting the scale model are: (1) the aerodynamic performance of the VAWTs has been obtained by the wind tunnel test and can be act as a validation test; (2) for general laws and parametric studies, the numerical simulation of the reduced scale VAWT model that can be regarded as a numerical simulation test is able to reflect the real characteristics and laws. Fig. 1 shows the geometric model of an H-rotor floating VAWT and the 6-DOF motions of a floating wind turbine faced with the wind and wave loads. The geometric parameters for the present wind turbine are listed in Table 1.

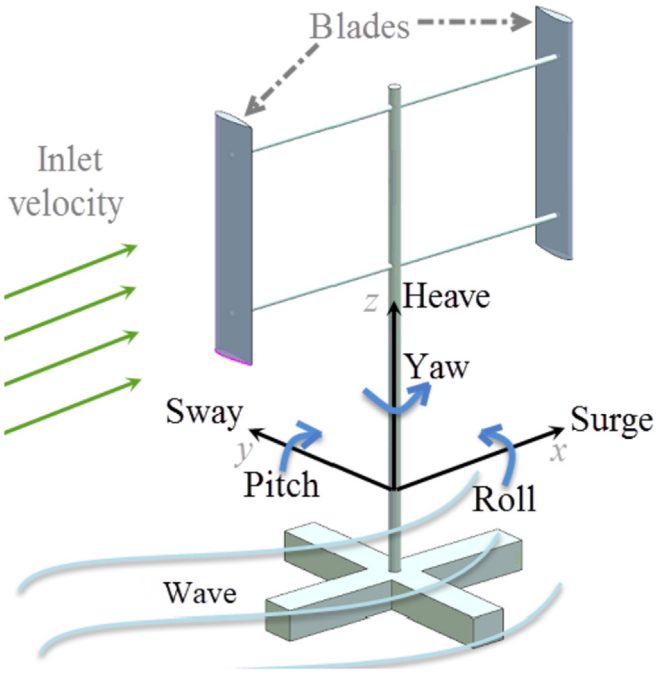

Fig. 1. Six-Degrees of freedom (6-DOF) for an offshore floating VAWT under wind and wave loads.

Table 1
Basic geometric parameters for the present H-rotor wind turbine [36].

Property	Value
Blade airfoil	NACA 0021
Blade number (N)	2
Span length (H)	1.200 m
Chord length (c)	0.265 m
Pitching angle (β)	6°
Rotor diameter (D)	2.000 m

3. Numerical simulation

3.1. Numerical method

As discussed above, the CFD method that can more accurately predict the aerodynamics of VAWTs has been widely used in analyzing the aerodynamic force, performance, and wake characteristics of wind turbines in recent years [37,38]. Thus, the CFD method is employed in the present study. For the CFD method, the URANS, LES, and DNS (direct numerical simulation) are the three main approaches to solving the Navier–Stokes equations. The huge amount of computation required for the DNS method hindered its applications in the flows with a high Reynolds number. Compared to the URANS method, the LES also needs a large amount of computation [39]. In view of the computational accuracy and resource, the improved delayed detached eddy simulation (IDDES) which combines the LES approach with the RANS model, is selected in the present simulation. Based on the delayed detached eddy simulation, the IDDES method integrated into the SST k-ω model is able to more effectively resolve turbulence activity close to the wall when compared with the pure DES model [40]. In the authors' previous study, the IDDES method could predict the power coefficient and wake velocity of H-rotor wind turbines with good accuracy [16]. The IDDES method has been implanted into the commercial CFD software STAR-CCM+ [41], which is a Finite Volume Method based solver, and will be employed in this study.

In the IDDES approach, the modified shear stress transport (SST) k-ω is used for the part of the RANS model [40]. The length scale in the dissipation term in the transport equation is replaced with a hybrid length scale, and the turbulent kinetic energy equation can be written as [41]:

$$\frac{\partial(\rho k)}{\partial t}+\frac{\partial(\rho u_j k)}{\partial x_j}=\frac{\partial}{\partial x_j}\left[\left(\mu+\frac{1}{\sigma}\mu_t\right)\frac{\partial k}{\partial x_j}\right]+\tau_{ij}S_{ij}-\frac{\rho k^{3/2}}{l_{HYBRID}} \tag{1}$$

where ρ, k, u_j, t, μ, μ_t, τ_{ij}, and S_{ij} are the density, turbulent kinetic energy, velocity, time, molecular viscosity, turbulent viscosity, tensor of stress, and mean strain rate, respectively. The l_{HYBRID} is the IDDES length scale, written as:

$$l_{HYBRID}=\tilde{f}_d(1+f_e)l_t+\left(1-\tilde{f}_d\right)C_{des}\Delta_{IDDES} \tag{2}$$

where C_{des} is a model constant for DES, Δ_{IDDES} is the mesh length scale of IDDES, and can be written as:

$$\Delta_{IDDES}=\min(\max(0.15d,0.15\Delta,\Delta_{\min}),\Delta) \tag{3}$$

$$l_t=\sqrt{k}\Big/\beta^*\omega \tag{4}$$

$$\tilde{f}_d=\max((1-f_{dt}),f_B) \tag{5}$$

$$f_e=\max((1-f_{dt}),f_B)\psi f_{e2} \tag{6}$$

where β^* is a constant, which is equal to 0.09 in the SST k-ω model, Δ is the grid scale, and $\Delta_{\min}$ is the smallest distance between the cell center under consideration and the cell centers of the neighboring cells.

3.2. Computational domain and mesh topology

As shown in Fig. 2 (a), the global computational domain is a cube, which has the enough cross-sectional area perpendicular to the direction of inflow and the long distance in the direction of inflow so as to effectively obtain fully developed wake structures. The length, width, and height of the global computational domain are 26D, 6D, and 5H, respectively. To realize the pitch and surge motions of the wind turbine in the global computational domain, the overset mesh will be utilized in the simulation. Overset mesh means the computational domain with several different meshes that overlap each other in an arbitrary manner, and it is suitable for solving moving bodies [41]. Thus, in the present study, the overset mesh is set as a cylinder located in the cuboid computational domain as shown in Fig. 2 (a). The diameter and height of the overset cylinder are 1.6D and 1.5H, respectively. This size setting can not only meet the requirements of mesh refined, but also reduce the unnecessary grid increase. The overset cylinder can be realized pitch and surge motions by the presetting rules of motion during the calculations. In an overset mesh, cells are grouped into active, inactive, or acceptor cells. Within active cells, discretized governing equations are solved. Within inactive cells, no equation is solved, however, these cells can become active if the overset region is moving. Acceptor cells separate active and inactive cells in the background region and are attached to the overset boundary in the overset region. Acceptor cells are used to couple solutions on the two overlapping grids. Variable values at donor cells of one mesh express variable values at acceptor cells in the other mesh, through interpolation. The donor cells are the active cells from the other mesh that are nearest to the acceptor cell. Then, the suitable

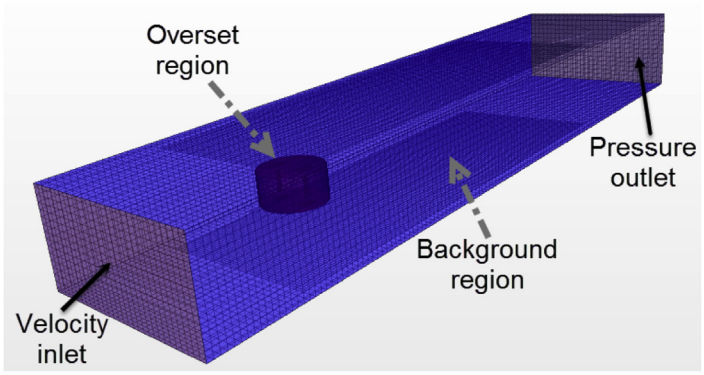

(a)

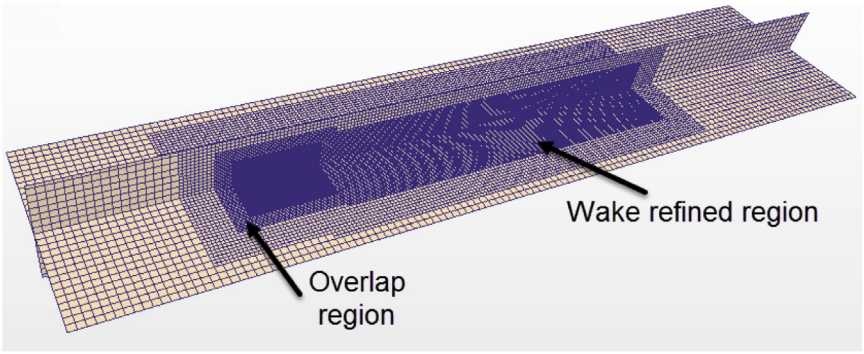

(b)

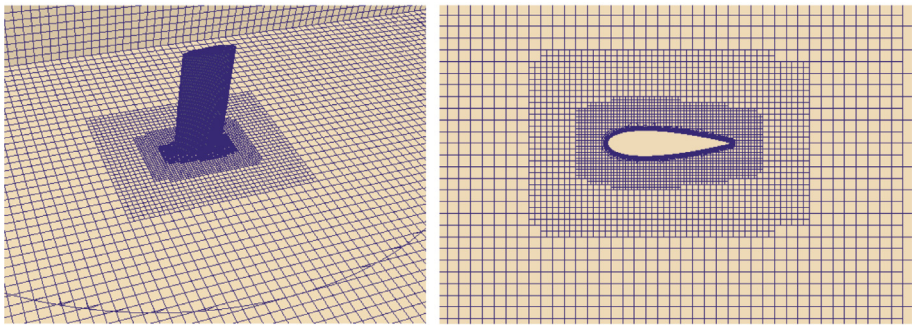

(c) (d)

Fig. 2. Computational domain and mesh topology for the present CFD model: (a) 3D computational domain; (b) two orthogonal sections for the computational domain; (c) mesh topology around the blade; (d) boundary layer grids.

interpolation method is selected for the data exchange.

Fig. 2 (b)~(d) show the grid topology in some typical cross sections. Fig. 2 (b) shows the mesh topology of two orthogonal middle sections. Two mesh refined regions that are close to the blades region and in the wake region should be generated. The mesh density in these two regions is refined and is beneficial to more accurately predict the aerodynamic forces and wake velocity. Fig. 2 (c) depicts the mesh size between the overset boundary and the overlap region. Overlap is an artificial region that can provide sufficient space for the movements of the overset region. The mesh size at the overset boundary and in the overlap region should be set as the same. Thus, the data exchange between these two regions at each iteration is more efficient. The method of the data exchange chooses linear interpolation, because it is more suitable for moving boundary conditions and could avoid overlapping of the interpolation elements. The refined mesh around the blade and the boundary layer grid are shown in Fig. 2 (c) and (d). There are 108 and 126 cells distributing around the chordwise and along the spanwise, respectively. Meanwhile, the boundary layer prismatic grids are generated to better predict the velocity and pressure gradients. Based on the inlet velocity (8 m/s) and the chord length ($c = 0.265$ m), the *Re* (Reynolds number) is about 1.62×10^5–2.89×10^5 in this simulation. According to the requirement of the IDDES turbulence model, the thickness of the first layer in the boundary layer prismatic grids is set as 2×10^{-5} m to meet $y^+<1$. As shown in Fig. 2 (d), the total thickness of the boundary layer is 0.01 m with a growth rate of 1.20. The mesh independent validation for the present mesh topology will be

conducted in the next section.

3.3. Solver setting

In this simulation, the Mach number is always below 0.3, thus the incompressible flow and segregated flow models are chosen in the transient flow [42]. The implicit unsteady approach is selected to solve the discrete Navier-Stokes equations. The convection term selects the second-order upwind scheme, which is more suitable for solving the incompressible N-S equations with the SST k-ω based model [43]. The temporal discretization uses the second-order central difference scheme. According to the author's previous study [16], the time step that is set as the requirement time of the azimuth angle of $\pi/90$ of the rotor rotation can obtain accurate aerodynamic forces. In each time step, the number of inner iterations is set as 20. The total physics time needs to be set as the requirement time of 12–16 revolutions of the rotor so as to ensure that the wake is fully developed. All the calculations in this research are run on two small servers, and each of them has two Intel (R) Xeon (R) CPUs (E5-2630 v3), a 4TB hard drive, and 128 GB of memory.

For the boundary conditions shown in Fig. 2 (a), the outlet condition is set as the pressure outlet with a relative pressure of $p_0 = 0$. The four sides of the global computational domain are set as the slip wall, which means that the viscous shear force at the wall boundary face is equal to zero. The boundary surfaces of the overset region are the overset mesh boundary, which can exchange data with the outer region at each iteration. At the inlet condition, the atmosphere boundary layer is considered, with the assumption that the inlet velocity is an exponential velocity profile with a moderate turbulence intensity of 8%. The velocity of the shear flow on the inlet boundary can be defined as [44]:

$$V_\infty = V_0 \times (z/H_0)^\alpha \tag{7}$$

where V_0 is the velocity at the reference height, H_0 is the reference height, z is the relative height above H_0, and α that is the power exponent is equal to 0.12 corresponding to the ocean area.

For the pitch and surge motions, the motion rules should be preset into the STAR-CCM + by using the user defined functions (UDFs). The pitch and surge motions of the wind turbines is mainly induced by the wave load. The previous studies showed that the pitch and surge motions of the wind turbine can be regarded as simple harmonic motion and conform to the law of sine [4,34,35]. The rotation axis of the pitch motion is parallel to the y-coordinate and located at the bottom of the overset region. The direction of motion for the surge is always parallel to the x-direction. Thus, the generalized displacements of the pitch and surge motions can be represented as:

$$\beta_p = A_p \cdot \sin\left(2\pi f_p t\right) \tag{8}$$

$$S_s = A_s \cdot \sin(2\pi f_s t) \tag{9}$$

thus, the pitching angular velocity (ω_p) and the surging velocity (v_s) can be written as:

$$\omega_p = 2\pi f_p A_p \cdot \cos\left(2\pi f_p t\right) \tag{10}$$

$$v_s = 2\pi f_s A_s \cdot \cos(2\pi f_s t) \tag{11}$$

where, β_p, A_p, f_p, S_s, A_s, f_s and t are the pitching angle, pitching amplitude, pitching frequency, surging displacement, surging amplitude, surging frequency and time, respectively.

4. Verification and validation

The quality of the mesh and validity of the CFD model can directly affect the efficiency and precision of the results of the numerical simulation. In this section, these two parts are tested by comparing with the experimental data from the available wind tunnel test [36]. The inlet boundary condition adopts the certain settings from the original experiment rather than the shear flow, i.e., the inlet velocity is uniform flow (8 m/s) with the turbulence intensity below 1%.

4.1. Mesh dependency

For the purpose of the present study, obtaining the most accurate wake velocity requires the dense mesh to be behind the wind turbine. Furthermore, a reasonable grid number around the blade can affect both the aerodynamic forces prediction and downstream velocity distribution. Thus, six grid topologies, of which the main differences are the grid numbers around the blade or at the wake region, are generated and listed in Table 2. As shown in Table 2, the grid numbers around the blades are different among Mesh 1 to Mesh 4, and grid numbers at the wake region are different among Mesh 2, Mesh 5 and Mesh 6. It can be seen that at a low grid density (Mesh 1), the predicted power coefficient (C_p) is less than that predicted by other mesh topologies. The discrepancy of C_p between Mesh 2 and Mesh 3 is just about 0.91%. Further increasing the grid number in the overset region to 4,809,875, the value of C_p almost no longer changes. Considering the precision requirements and computing resources, the grid number in the overset region being equal to 2,702,825 is preferable. Fig. 3 depicts the wake profiles of the wind turbine in the conditions of Mesh 2, Mesh 5, and Mesh 6, respectively. It can be seen that the wake profiles predicted by Mesh 2 and Mesh 6 are almost identical. However, the wake profile predicted by Mesh 5 shows a distinct difference compared to the other two mesh topologies. Considering the predicted results of C_p and the wake profile, Mesh 2 can be regarded as a reasonable grid division, which can balance the efficiency and precision.

Table 2
Mesh dependency test based on the errors of the power coefficients at TSR = 2.517.

Mesh number	Total number of grid	Number in overset	Number in background	Predicted Torque [N·m]
Mesh 1	3,079,677	1,589,875	1,489,802	5.208
Mesh 2	4,955,476	2,702,825	2,252,651	5.689
Mesh 3	6,173,437	3,920,786	2,252,651	5.741
Mesh 4	7,062,526	4,809,875	2,252,651	5.751
Mesh 5	3,526,717	2,702,825	1,087,635	5.609
Mesh 6	5,528,084	2,702,825	3,889,002	5.684

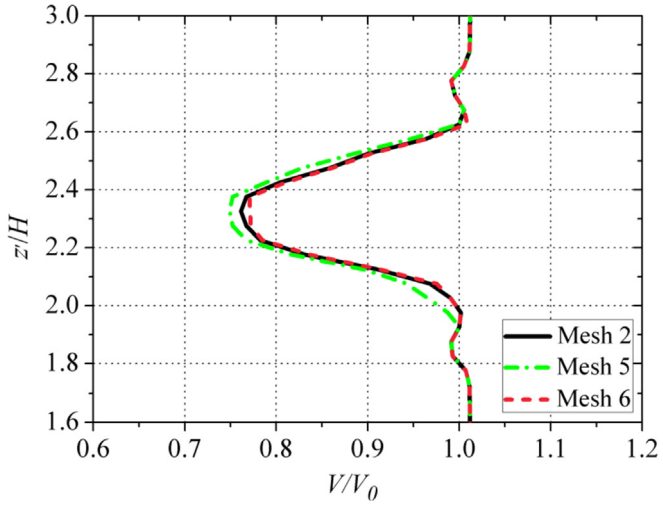

Fig. 3. Mesh independence validation based on three different mesh topology by using the normalized wake profiles at downwind distance of $x = 7D$ for the wind turbine, where Mesh 2, Mesh 5, and Mesh 6 have 4,955,476, 3,526,717 and 5,528,084 cells, respectively.

4.2. Validation

The comparisons of the power coefficient and the near wake velocity between available experiments and numerical simulations are demonstrated in this section. The power coefficient reflects the generating efficiency of the wind turbine, and it is also a measurement of the torque of the rotor to some extent. Fig. 4 (a) compares the values of C_p between experiments and simulations at five tip speed ratios (TSRs) [36]. The relative errors at the lower and higher TSRs show larger values than those at medium TSRs. The maximum error of 23.46% occurs at TSR = 0.750. Moreover, the wake profiles of the wind turbine at a downwind distance of $x = 1D$ at two TSRs are compared in Fig. 4 (b) and (c) [36]. It can be seen that the errors between experiments and simulations are larger in higher TSRs, especially in the centerline position. However, the wake profiles agree well with the experimental values. There are some factors, such as neglected support arms, unconsidered mechanical energy loss, failure to check for some grid defects, and defects of the essential characteristics of the turbulence model, that also have some effects on the power and wake predictions. The prediction accuracy for the present CFD model is adequate for the study of the influences of variable parameters on wake characteristics in this paper. Thus, it can be act as a valid model to perform the following parameter studies.

Similar validation work was performed in Ref. [16]. One difference between the numerical model in the current study and in Ref. [16] is that the trim cell is utilized to mesh the fluid domain while the polyhedral cell was adopted for the meshing work in Ref. [16].

5. Results and discussions

Pitch and surge motion are two main movements of floating wind turbines when they are faced with wind and wave loads. These two motions can be treated as periodic motions with the sinusoidal rule as shown in Eqs. (8) and (9) [34]. In addition, to more clearly analyze the simulation results, two conditions are set in the simulations: (1) the rotor's angular velocity (ω) is a constant at 17.959 rad/s, namely TSR = 2.245; (2) the pitching periods (T_p) and surging periods (T_s) are the integral multiple of the periods (T) of the rotor rotation.

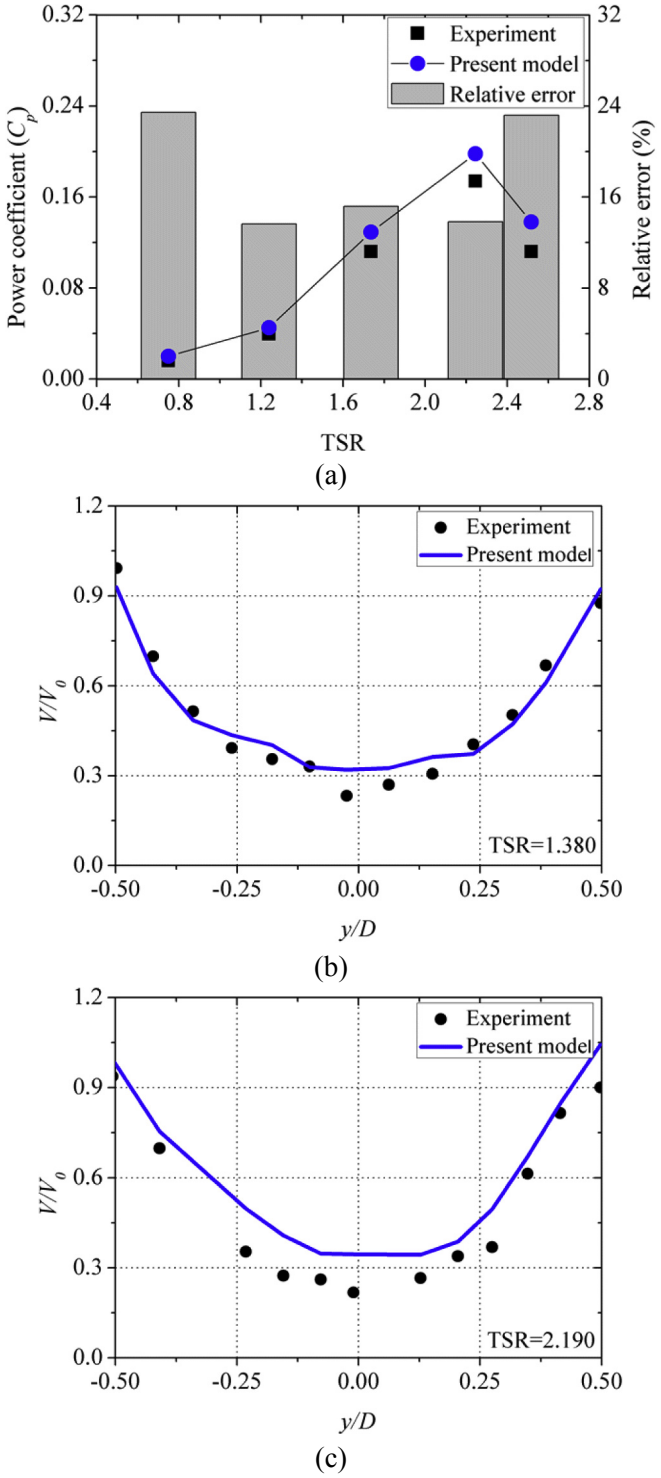

Fig. 4. Validation of the CFD model between the simulations and the experiments [36]: (a) Comparison of power coefficients at different TSRs; (b) Comparison of average wake velocity at $1D$ and TSR = 1.380; (c) Comparison of average wake velocity at $1D$ and TSR = 2.190.

5.1. Wake characteristics in pitch motion

Although pitch motion is induced by the joint action of wind and wave loads, the pitching angle is limited to a certain extent so as to ensure the safety of the platform. According to the study of Collu et al. [45], the maximum pitching angle of the platform for

VAWTs should be designed not to exceed the angle of ±15°. Thus, the pitching amplitude is set as 15° and the pitching period T_p is set as four times the rotation period (T) of the wind turbine.

The platforms' pitch motion is equivalent to increase the relative velocity between the wind turbines and the inflow wind. The induced velocity can make varying degrees of variation in the aerodynamic forces and wake structures for the wind turbines [46]. Therefore, there must be some effects of the pitch motion on the distribution of the wake velocity, which thereby influences the operating efficiency of the neighboring wind turbines in the wind farm. Fig. 5 shows the wake profiles of the wind turbine in pitch and non-pitch conditions, where wake profiles at four critical time nodes in pitch motion, namely 1/4T_p, 2/4 T_p, 3/4 T_p and 4/4 T_p, are compared. In all downwind distances, the peak values of the wake profile in pitch motion are smaller than those in non-pitch conditions. The ranges of the wake deficit in the vertical direction are widened at each downwind position in pitch motion, and it becomes wider as the downwind distances increase. Pitch motion not only increases the velocity deficit, but also changes the direction of the evolution of the wind turbine wake. The centerlines of the wake profiles at each pitching state always alternately appear below or above the midpoint of the rotor (baseline) in the vertical direction. Comparing the six subfigures, it can be clearly seen that the offsets of the centerline away from the baseline become larger when the downwind distances are increased. As shown in Fig. 5 (a), (b), and (c), in the near-wake region, the dispersion degrees of the main

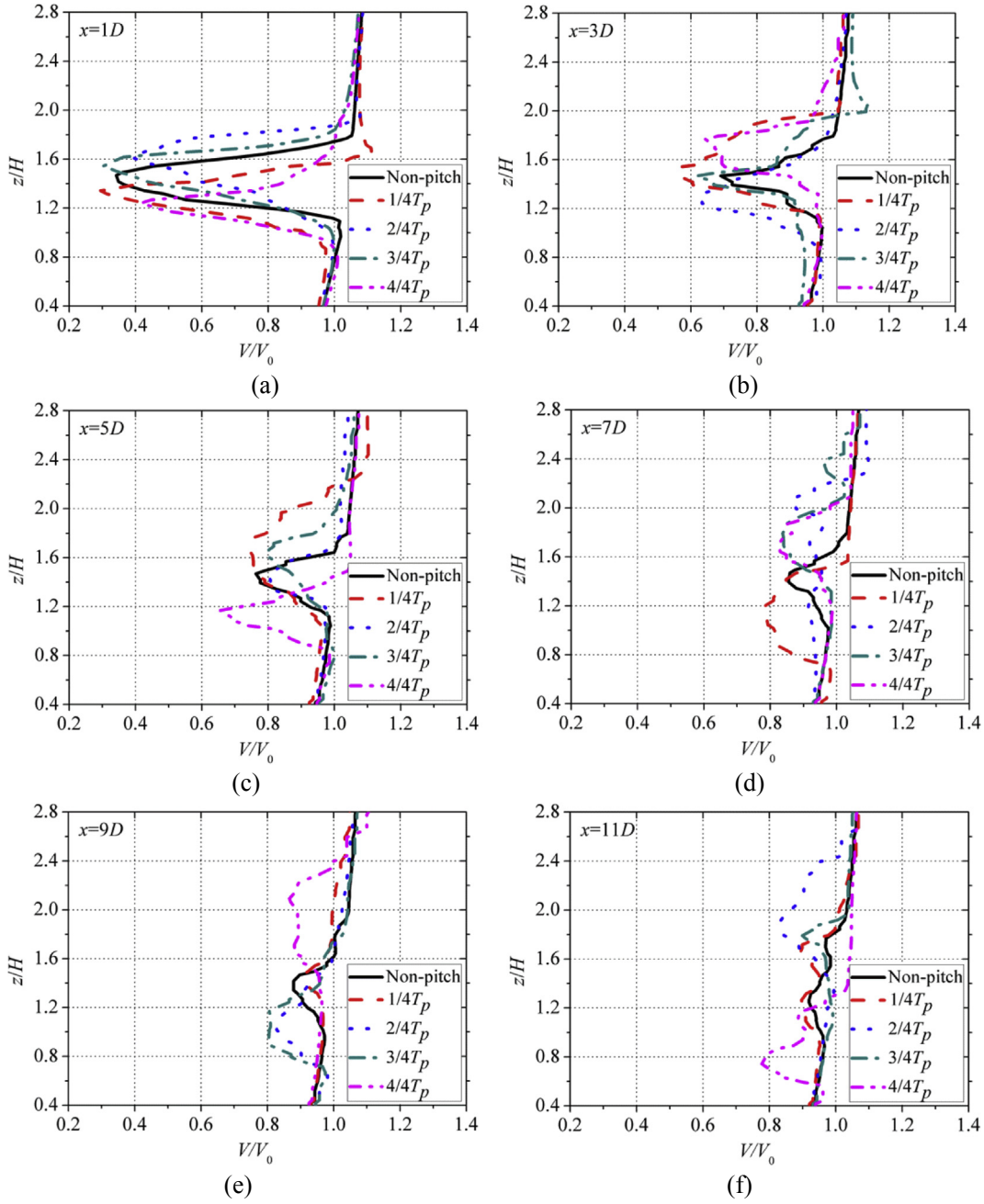

Fig. 5. Vertical profiles of the normalized wake velocity through the rotation axis of the wind turbine at six downwind distances between non-pitch condition and four critical pitching stages. (1/4T_p and 3/4T_p are the times of wind turbine locating at the positions of maximum positive and negative amplitudes, respectively. 2/4T_p and 4/4T_p are the times of wind turbine passing the equilibrium position with negative and positive additional velocities, respectively.)

stream of the wake at pitching states of $1/4T_p$ and $3/4T_p$ (the rotor is located at the position of maximum amplitude) is more severe than those at pitching states of $2/4T_p$ and $4/4T_p$ (the rotor is through the balance position). Whereas, the influence of pitch motion on wake profiles is more obvious at the pitching states of $2/4T_p$ and $4/4T_p$ in the far-wake region (see Fig. 5 (e) and (f)). At the transition position from near-wake to far-wake regions (Fig. 5 (d), $x = 7D$), the wake profiles at each pitching state all show distinct differences when compared to the non-pitch condition. The wake profiles of the wind turbine are formed by the perturbation of the rotor's rotation in non-pitch condition, but they can be regarded as the results induced by the resultant motion of combining the swing and rotation in pitch motion. Because of the existence of the additional swing in pitch motion, the wake development is changed obviously in the platform's pitch motion.

To more clearly observe the development and evolution of the wake structure for the H-rotor wind turbine during one pitching period, the comparison of wake structures between non-pitching and pitch conditions is demonstrated in Fig. 6. Fig. 6 (a) shows the wake structures of the wind turbine in non-pitch condition. It can be seen that the core zone of the wake presents a straight line in the near-wake region ($x = 1$~$5D$) and a wavy line in the far-wake region ($x > 5D$). The contour of the core zone of the wake in the vertical direction almost entirely locates in the scope of the height of the blades spanwise. Meanwhile, the effect of shear flow on the wake region is still clear beyond the core of the wake along the blades spanwise. Comparing the wake structures in non-pitch and pitch motions, a significant change of development of the wake can be observed. In all of the four critical states, the fluctuation of the core zones of the wake is more violent than that in non-pitch condition. The contours of the core wake all exceed the scope of the blades spanwise and the excess range even reaches the height of the blades. Moreover, the pitch motion can more intensely disturb the velocity distribution in the wake region due to the influence of the additional swing motion of the wind turbine. The additional strong interaction between the wind and the rotor also can make the effect of the velocity gradient in the wake region no longer obvious beyond the core zone of the wake along the blades spanwise. In Fig. 6 (b), the wind turbine moves to the right amplitude position. In the near-wake region, it can be found that the main

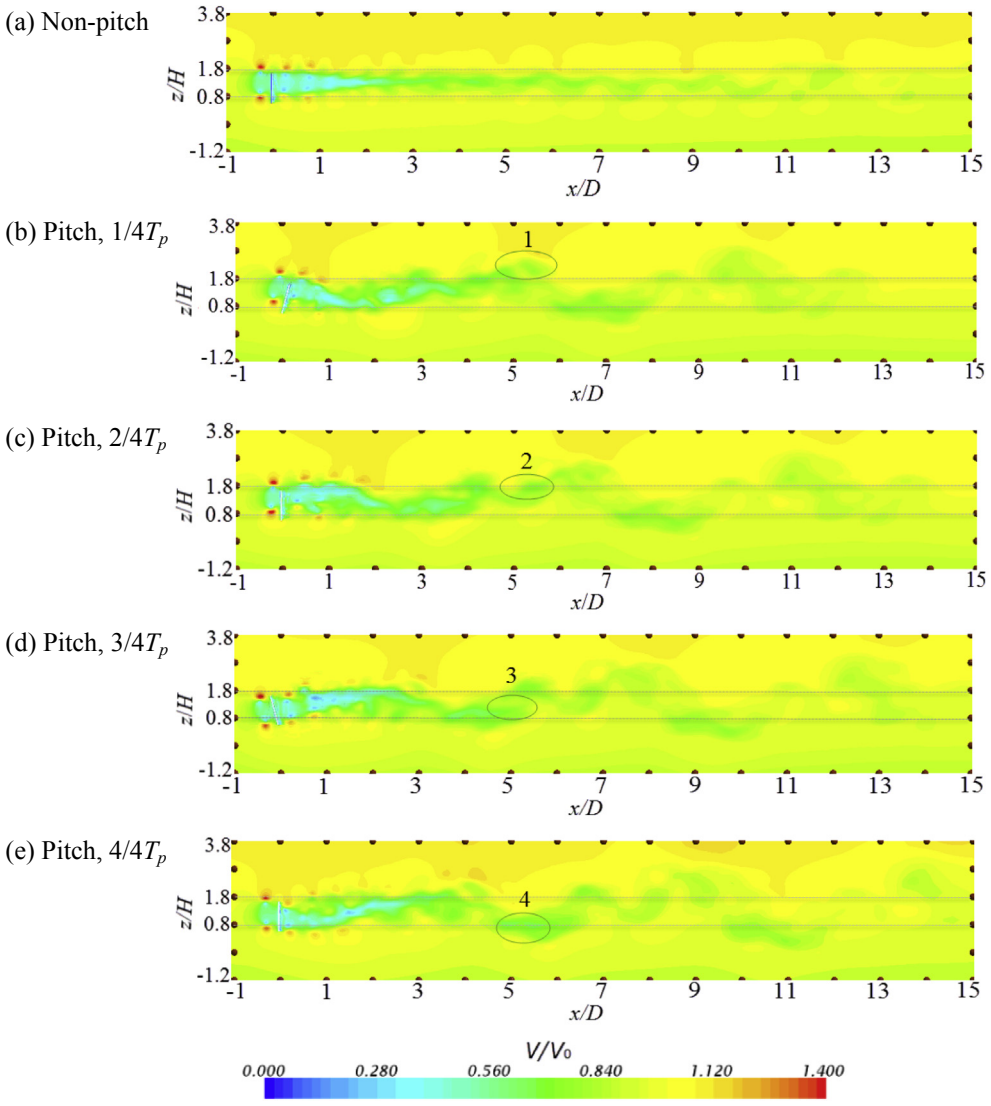

Fig. 6. Contours of the normalized wake velocity in the vertical plane through the rotation axis of the wind turbine between non-pitch condition and four critical pitching stages. ($1/4T_p$ and $3/4T_p$ are the times of wind turbine locating at the positions of maximum positive and negative amplitudes, respectively. $2/4T_p$ and $4/4T_p$ are the times of wind turbine passing the equilibrium position with negative and positive additional velocities, respectively.

stream of the wake is obviously skewed downward due to the right tilt angle of the rotor. As shown in Fig. 6 (c), the downward wake contour in the near-wake region will change to the horizontal direction when the rotor moves to the left through the equilibrium position. In this state, the relative speed between the wind and the rotor is maximum. At the time of $3/4T_p$, the wind turbine reaches the left amplitude position (see Fig. 6 (d)). The wake contour is skewed upward, which is also induced by the left tilt angle of the rotor. In Fig. 6 (d), the wake contour transforms horizontal again in the near-wake region when the rotor returns to the equilibrium position after one pitching period. It can be found that the reciprocating motion of the rotor causes the main stream of the wake to be skew downward and upward alternately. Thus, the core zone of the wake in the far-wake region is driven by the up-and-down main stream in the near-wake region and presented the obvious and violent fluctuation movement in the full wake stream. As shown in Fig. 6 (b)~(e), the circles 1, 2, 3, and 4 that like four mass points in the transverse wave of the wake periodically oscillate up and down as the progress of the pitch.

The wind turbines will generate pitch motion with different amplitudes and periods when they are faced with different wind and wave loads. How these working conditions affect the wake characteristics of the wind turbines is crucial for both platform design and wind field optimization. In this part, the wake profiles in three different pitching amplitudes, namely $A_p = 15°$, $10°$, and $5°$, are investigated. Fig. 7 shows the wake profiles at downwind distances of $1D$, $5D$, and $9D$ in four typical states for the three pitching amplitudes. As shown in Fig. 7 (a), (d), (g), and (j), in the downwind position of $x = 1D$, the values of the velocity deficit in the centerline position become larger and the offsets of the wake profile shifting downward and upward grow with the increase of the pitching amplitudes due to the incremental inclined angle of the wind turbine. In addition, the variations of relative velocity induced by additional swing motion are different in these three pitching amplitudes, which also changes the distribution of the wake velocity. Those regular effects on the wake deficit in the near-wake region are changed in the transition region ($x = 5D$) and far-wake region ($x = 9D$). Although the figures of the second and third columns in Fig. 7 show that the wake velocity no longer regularly changes with the variation of the pitching amplitudes, the offsets of the main stream for the wake also present the rule of fluctuation. The amplitudes (h_p) of those fluctuations in the main stream of the wake decrease as the pitching amplitudes A_p decrease (see Fig. 9 (a)~(c)). In actual wind farm optimization, the wake profile in the far-wake region has the most concern because the distance between two wind turbines is always large enough. In Fig. 7 (c), (f), (i) and (l), the magnitude and position of the centerline of the wake appear irregularly due to the fact that the intensity and the wave crest of the fluctuation for the wake structures are changed in different pitching amplitudes. From the simulation results, it can be seen that the varying pitching amplitudes have a great influence on the wake structures.

The pitching period of the platform for the wind turbine which is another key parameter, affects the aerodynamics of the platform's pitch motion. Fig. 8 shows the vertical normalized wake profiles of the wind turbine in three different pitching periods of $T_p = 2T$, $T_p = 4T$, and $T_p = 8T$. As shown in Fig. 8 (d) and (j), at the downwind distance of $x = 1D$, the wake deficit and the offset of the centerline for the wake in the lower pitching period ($T_p = 2T$) are larger than those in the higher pitching periods ($T_p = 2T$, $T_p = 8T$) when the rotor passes the equilibrium position. At the stage of maximum amplitude, the wake deficit and the offset of the centerline for the wake in the lower pitching period are no longer the largest. Observing Fig. 9 (c)~(e), it can be found that the main streams of the wake firstly shift downward at the downwind distance of $x = 1D$ in the conditions of $T_p = 4T$ and $T_p = 8T$. However, it has reached the nadir and lifted upward at the downwind distance between $0D$ and $1D$ when the pitching period is equal to $2T$. This phenomenon leads to the wake structures in the lower pitching period abnormally changing in the stage of the rotor passing the equilibrium position. Meanwhile, from Fig. 9 (c)~(e), it can be also observed that the 'wave length' (l_p) of the 'wake wave' and the total influenced distance in the wake region are shortened with the decrease of the pitching periods. Whereas, the lower pitching period can improve the amplitude of the 'wake wave' and result in a stronger fluctuation in wake structure for the wind turbine. Because of different degrees of fluctuation for the wake structure in different pitching periods, the wake profiles of these three pitching periods show no regularity that can enhance the difficulty of predicting wake by theoretical model in the far-wake region.

5.2. Wake characteristics in surge motion

In this section, the wake profiles and structures between surge and non-surge conditions will be compared. The surging amplitude is set as one over ten of the rotor diameter for the wind turbine [4]. The surging period T_s is set as four times the rotation period T of the rotor. Thus, the amplitude and period of the surge are $A_s = 0.02$ m and $T_s = 1.40$s, respectively. As shown in Fig. 10, the surge motion can markedly change the wake profiles of the wind turbine at any stage when compared to the non-surge condition. In this comparison, four crucial stages of surge motion $1/4T_s$, $2/4T_s$, $3/4T_s$ and $4/4T_s$ represent the time of the rotor being in the position of positive amplitude, passing the equilibrium position with maximum relative speed, being in the position of negative amplitude, and passing the equilibrium position with minimum relative speed, respectively. In Fig. 10 (a) and (b), the maximum wake deficit in surge motion almost has no change and the vertical widths of the wake deficit area are magnified in some stages and shortened in other stages. These variations of the wake profile in surge motion in the near-wake region have little impact on the wind farm design. However, it has a great influence on the wake development and evolution. It can be clearly seen that the changes of the wake profile in the far-wake region are more obvious than those in the near-wake region. As show in Fig. 10 (c)~(f), two extreme values always appear on the wake profile in the certain stage of surge motion. Besides, the vertical positions of the peak value of the wake profile are also changed with the development of the surge motion during one surging period. It is shown that the addition of relative velocity between the wind and the rotor induced by the surge motion aggravates the complexity of flow in the wake region and affects the wake development to a great extent.

Fig. 11 compares the wake structures of the wind turbine between the four stages of surge motion and the non-surge condition. Similar to the non-surge condition, the vertical section of the wake structures all of the four cases show the triangle and the vertical width of the core zone for the wake diminishing as the downwind distance increases in the near-wake region under surge motion. As shown in Fig. 11 (b)~(e), the distance of this diminishing zone in the x-direction is larger at $2/4T_s$ and $3/4T_s$. The additional instantaneous relative speed can cause periodic variations of the influenced area of the main stream in the near-wake region. Meanwhile, in Fig. 11 (b), a spindle shaped (circle 1) wake zone is formed at the downwind distance of $x = 3D$, and this 'Spindle' continually moves to the far-wake region with the progress of the surge motion, such as the center of the 'Spindle' located at $5D$ and $7D$ at $2/4T_s$ and $3/4T_s$, respectively (see Fig. 11 (c) and (d), circle 2 and circle 3). The strength of the core zone of the 'Spindle' that is represented by circles 1, 2, 3, and 4 is also gradually weakened with the developing

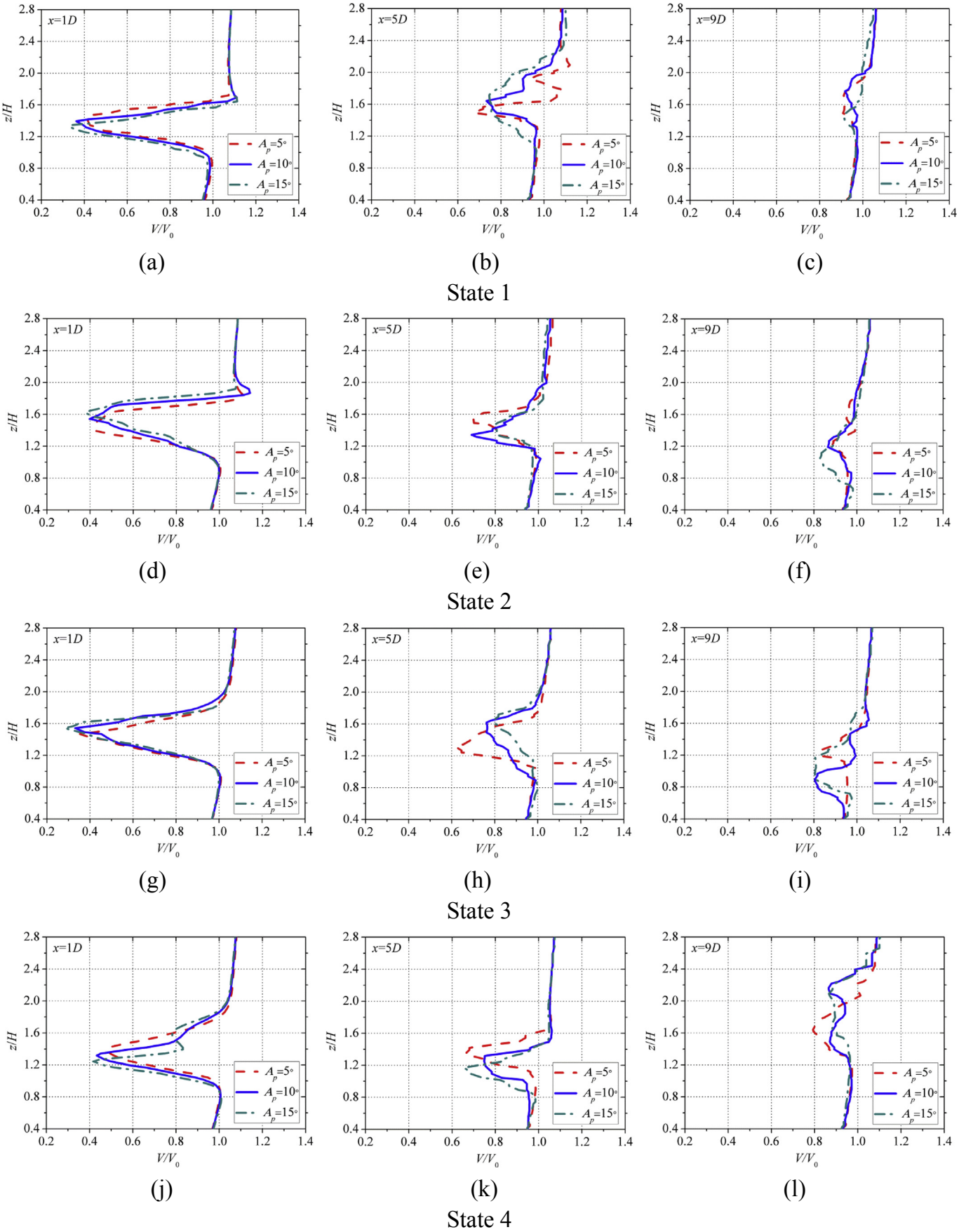

Fig. 7. Vertical profiles of the normalized wake velocity through the rotation axis of the wind turbine at three different pitching amplitudes. (State 1 and state 3 are the times of wind turbine locating at the positions of maximum positive and negative amplitudes, respectively. State 2 and state 4 are the times of wind turbine passing the equilibrium position with negative and positive additional velocities, respectively.)

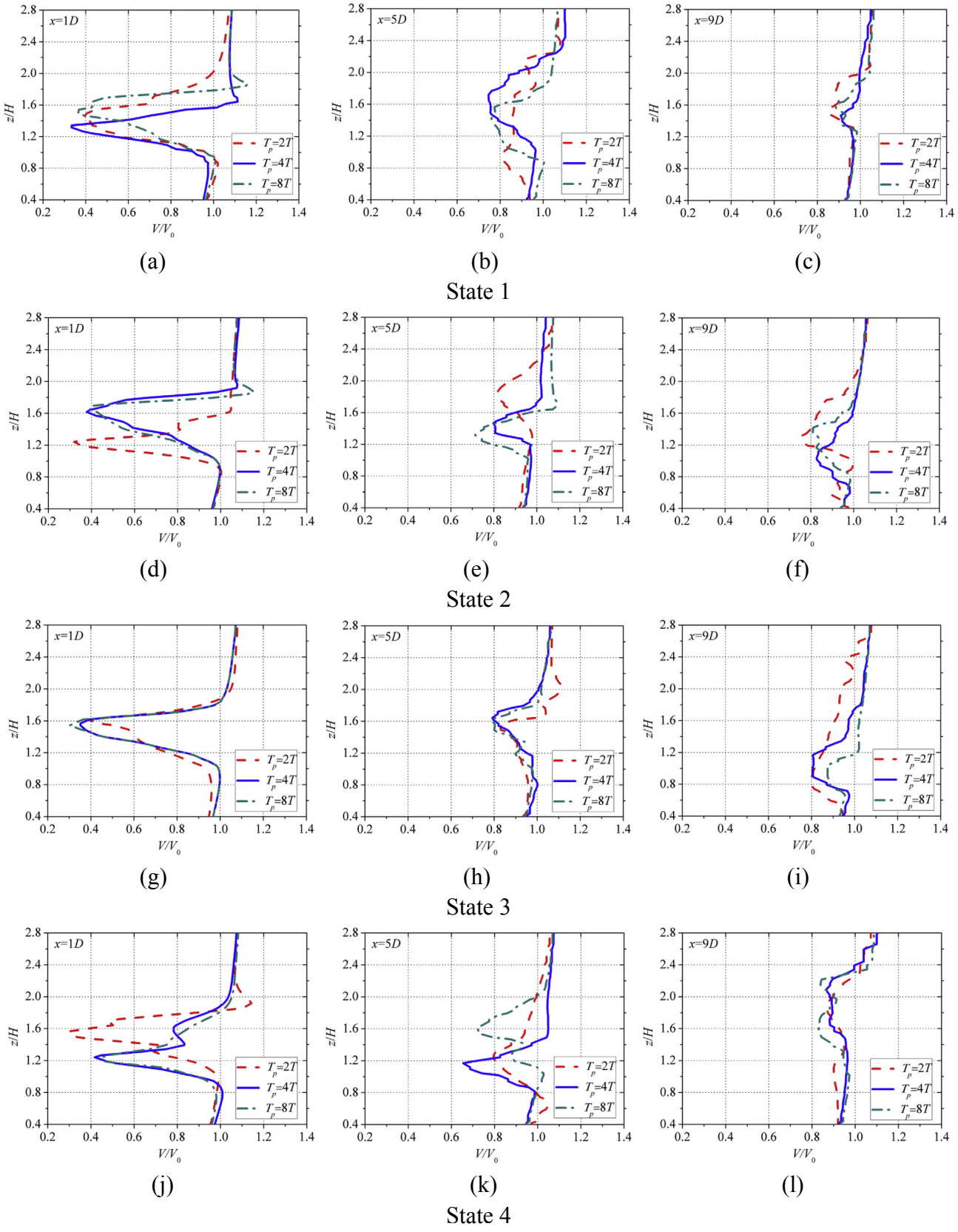

Fig. 8. Vertical profiles of the normalized wake velocity through the rotation axis of the wind turbine at three different pitching periods. (State 1 and state 3 are the times of wind turbine locating at positions of maximum positive and negative amplitudes, respectively. State 2 and state 4 are the times of wind turbine passing the equilibrium position with negative and positive additional velocities, respectively.)

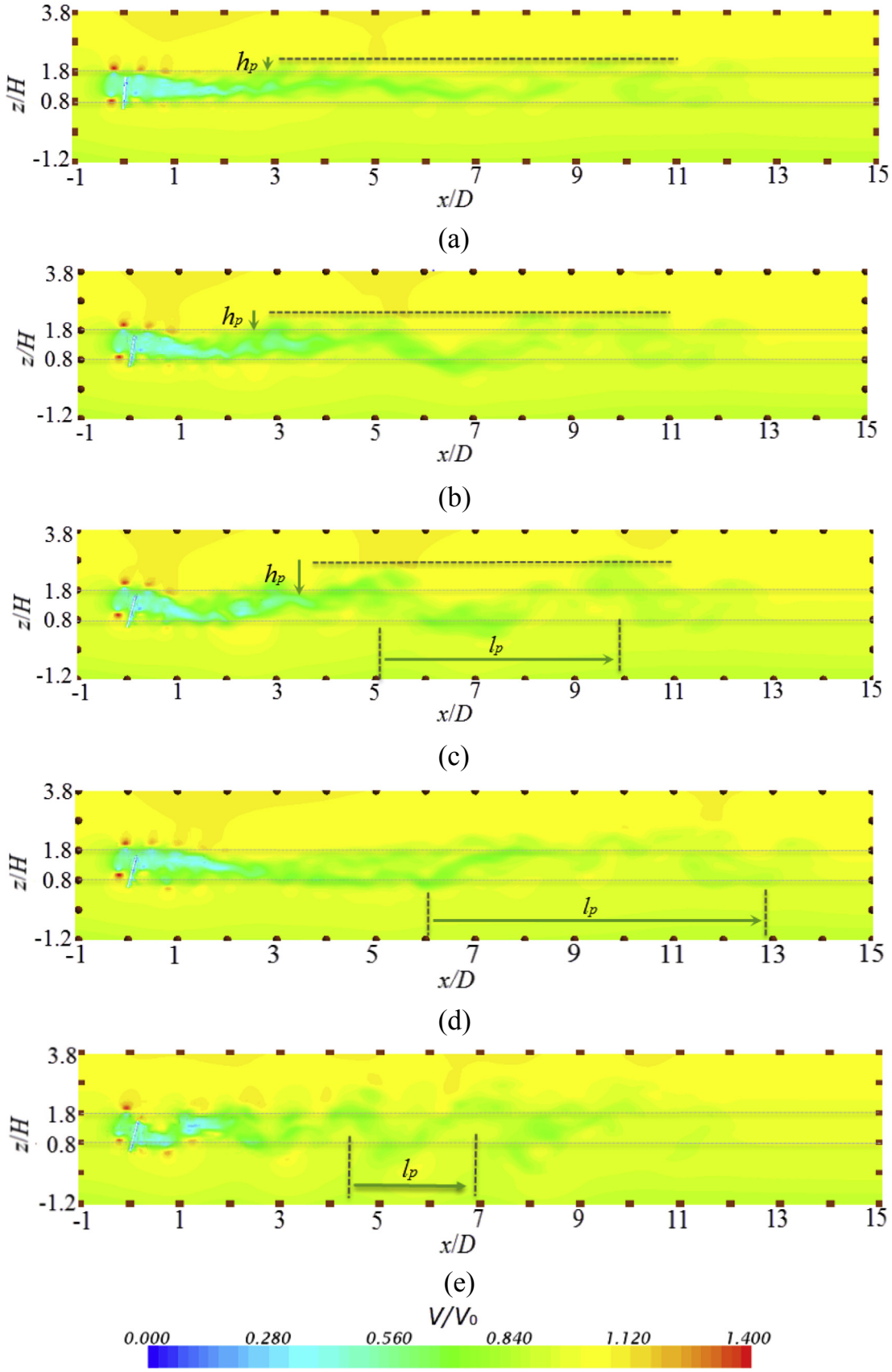

Fig. 9. Contours of the normalized wake velocity in the vertical plane through the rotation axis of the wind turbine in three different pitching amplitudes and pitching periods at state 1 (the time of wind turbine locating at the position of positive amplitude): (a) $A_p = 5°$, $T_p = 4T$; (b) $A_p = 10°$, $T_p = 4T$; (c) $A_p = 15°$, $T_p = 4T$; (d) $A_p = 15°$, $T_p = 8T$; (e) $A_p = 15°$, $T_p = 2T$.

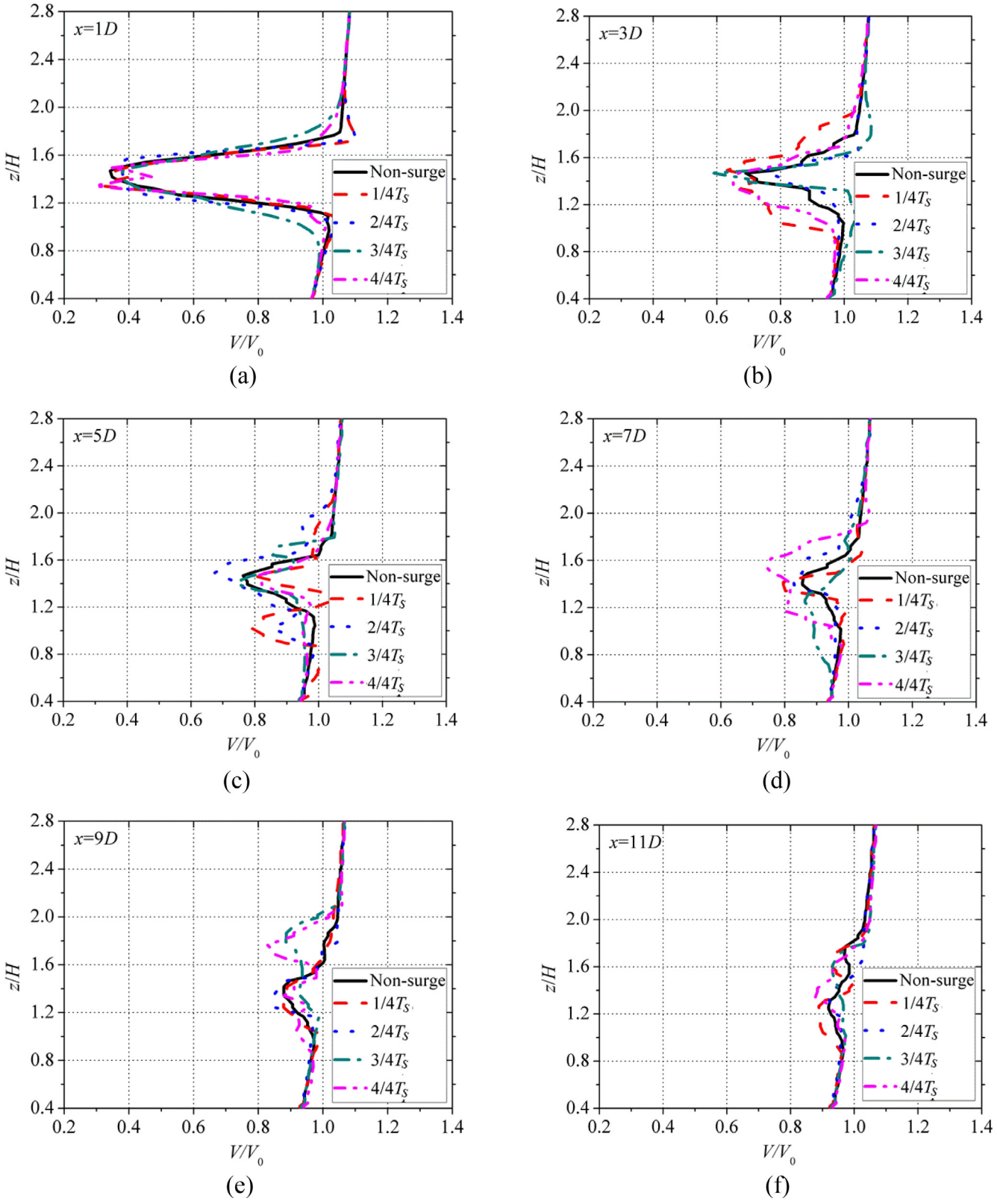

Fig. 10. Vertical profiles of the normalized wake velocity through the rotation axis of the wind turbine at six downwind distances between non-surge condition and four critical surging stages. ($1/4T_s$ and $3/4T_s$ are the times of wind turbine locating at the positions of maximum positive and negative amplitudes, respectively. $2/4T_s$ and $4/4T_s$ are the times of wind turbine passing the equilibrium position with negative and positive additional velocities, respectively.)

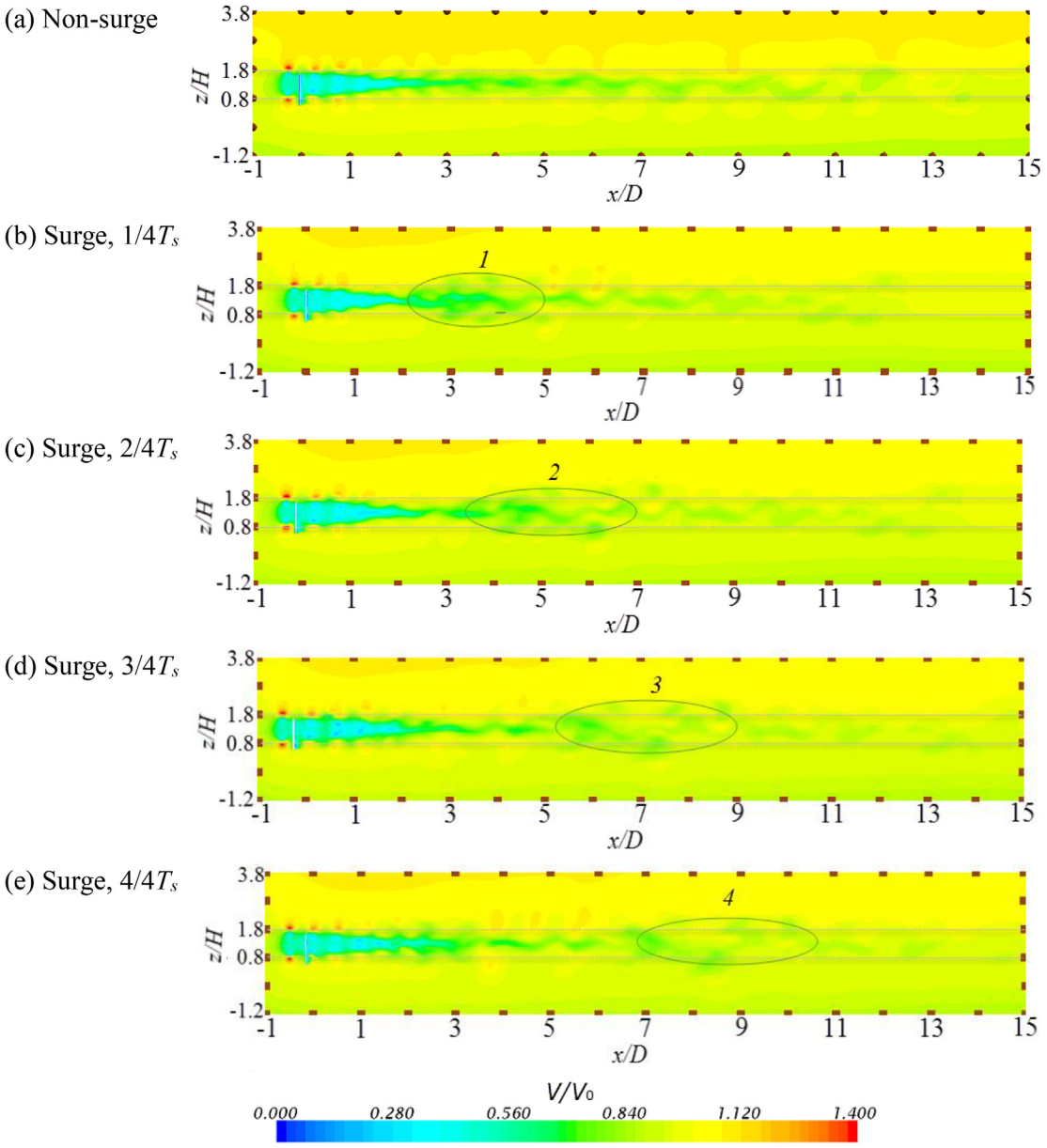

Fig. 11. Contours of the normalized wake velocity in the vertical plane through the rotation axis of the wind turbine between non-surge condition and four critical surging stages. ($1/4T_s$ and $3/4T_s$ are the times of wind turbine locating at the positions of maximum positive and negative amplitudes, respectively. $2/4T_s$ and $4/4T_s$ are the times of wind turbine passing the equilibrium position with negative and positive additional velocities, respectively.)

downwind distance until it disappears at the end of each surging period. The intricate wake profiles in the far-wake region shown in Fig. 10 are indeed generated by the periodic motion of the 'Spindle' associating with its damped strength during each surging period.

The additional velocity (V_{sa}) induced by the surge motion can increase or decrease the relative speed (V_{sr}) between the wind and the wind turbine. It also can change the inflow velocity of the rotor and affect the angle of attack of the blades [28]. The most important concern here is the influence of different surging amplitudes on the wake characteristics. Three surging amplitudes, namely $A_s = 0.20$, 0.14, and 0.08, and the same surging period of $T_s = 4T$ are set in the simulations. Fig. 12 plots the wake profiles of the wind turbine in these three cases. In the near-wake region (see Fig. 12 (a), (d), (g) and (j)), the wake direction and wake profiles are almost no different among these surging amplitudes. The velocity deficit at the centerline position is larger in the higher surging amplitude. Fig. 12 (a) and (j) show that an abrupt rise appears at the centerline position of the wake profile when the wind turbine is at the stages of $1/4T_s$ and $4/4T_s$ due to the fact that the value of V_{sr} is reduced by the larger V_{sa}. In the downwind distance of $x = 5D$, the wake profiles have obvious differences at the positions of the two maximum amplitudes and little discrepancy at the equilibrium position in these three cases. In the far-wake region, the wake profiles in these cases show very different forms as depicted in Fig. 12 (c), (f), (i) and (l). From Fig. 14 (a)~(c), it can be clearly seen that the stronger perturbation induced by larger V_{sa} in the high surging amplitude can cause the wake structure in the far-wake region to be more dispersive, and the core zone of the 'Spindle' more intumescent. The different degrees of initial perturbation occurring in the position of the wind turbine change the evolution of the wake structure, and the strength and moving velocity of the periodic 'Spindle' in the far wake region can directly affect the distribution of wake velocity.

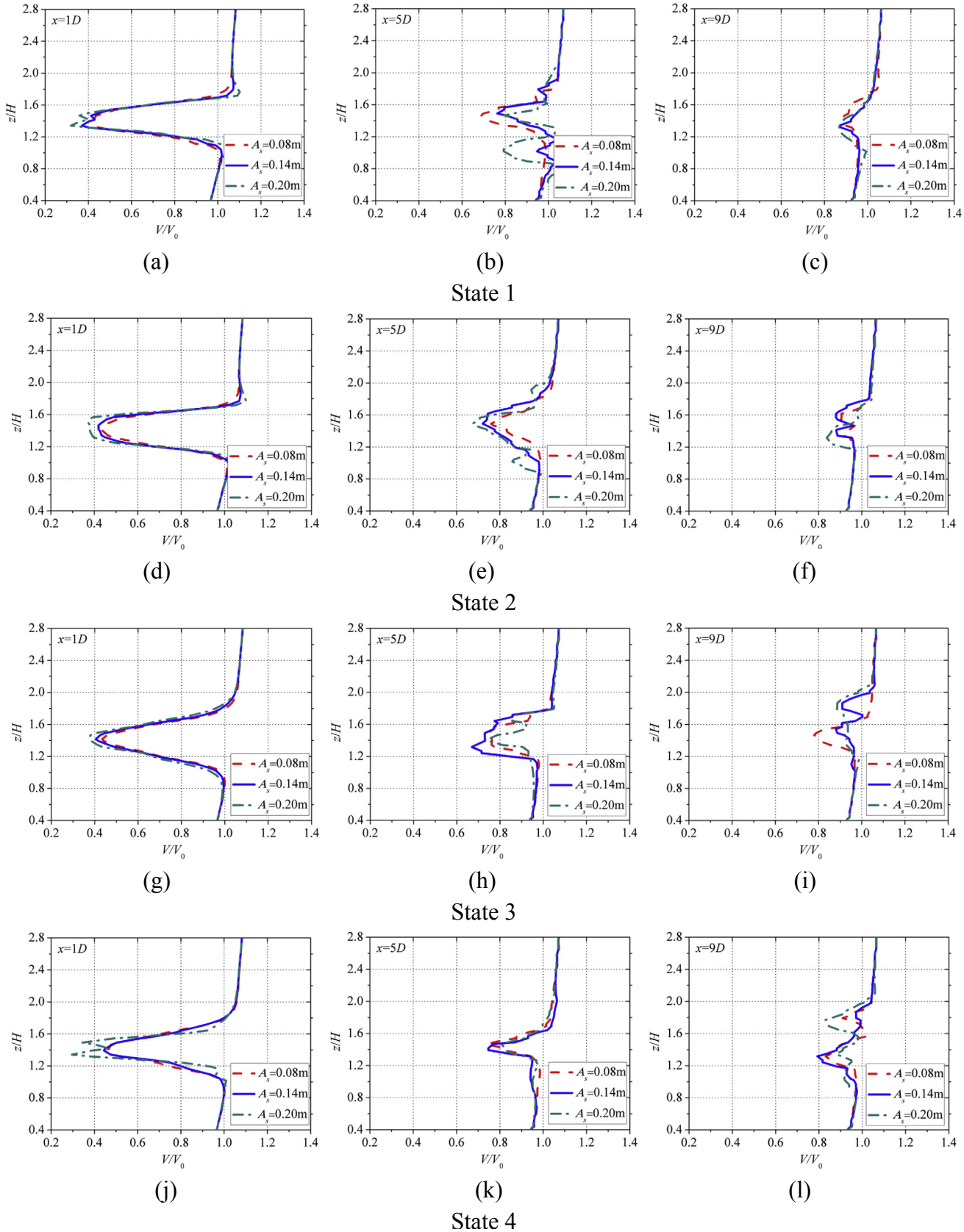

Fig. 12. Vertical profiles of the normalized wake velocity through the rotation axis of the wind turbine at three different surging amplitudes. (State 1 and state 3 are the times of wind turbine locating at the positions of maximum positive and negative amplitudes, respectively. State 2 and state 4 are the times of wind turbine passing the equilibrium position with negative and positive additional velocities, respectively.)

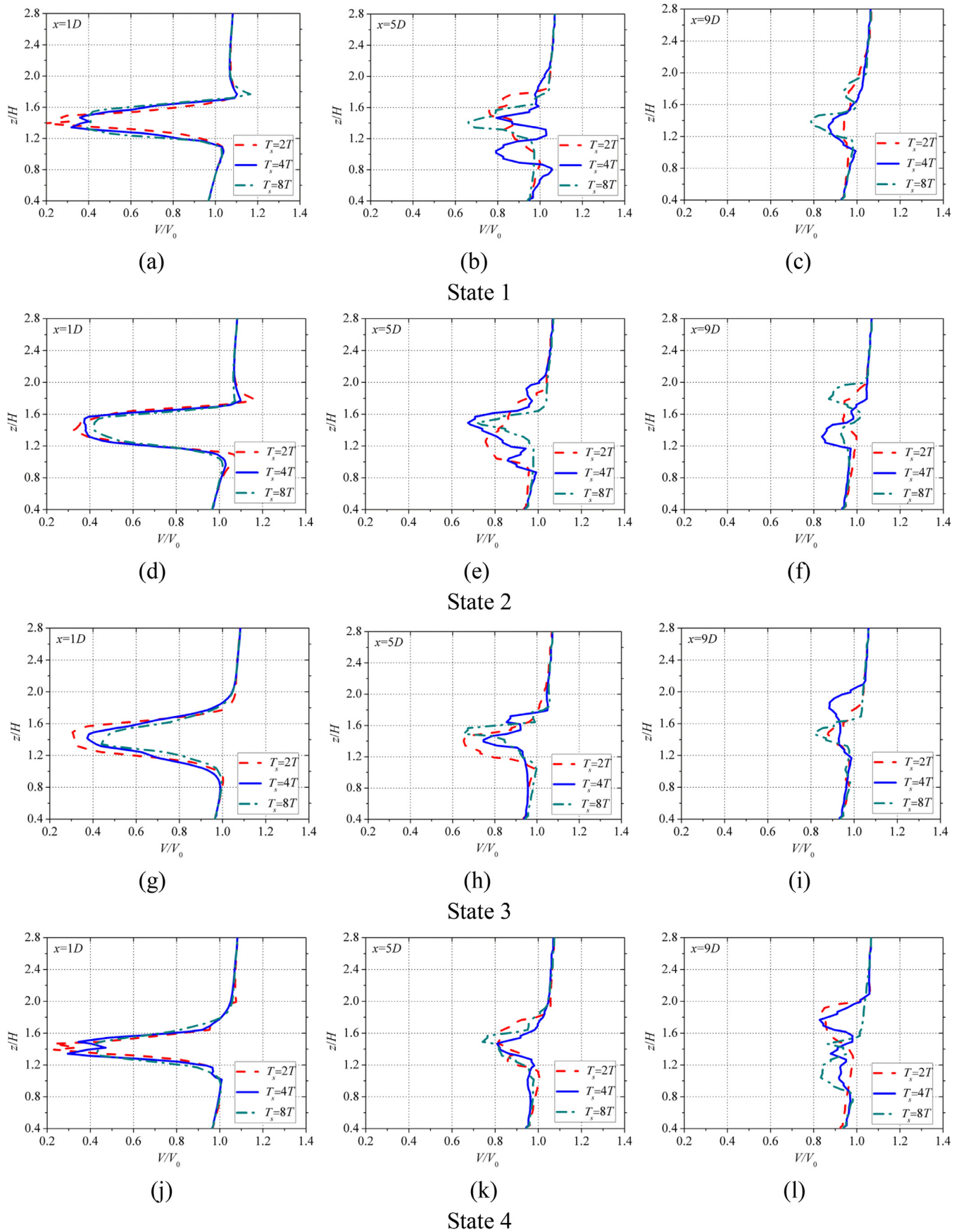

Fig. 13. Vertical profiles of the normalized wake velocity through the rotation axis of the wind turbine at three different surging periods. (State 1 and state 3 are the times of wind turbine locating at positions of maximum positive and negative amplitudes, respectively. State 2 and state 4 are the times of wind turbine passing the equilibrium position with negative and positive additional velocities, respectively.)

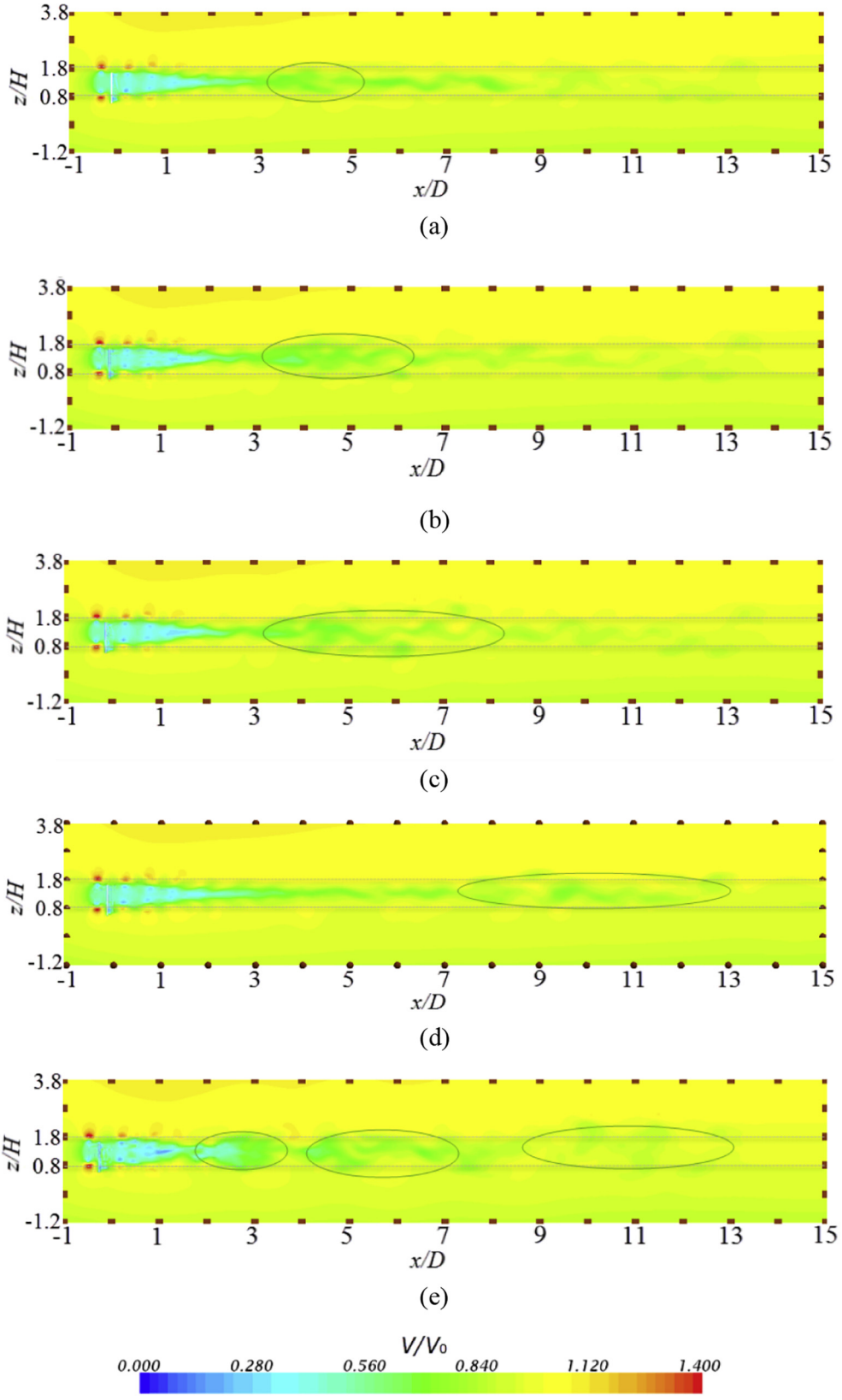

Fig. 14. Contours of the normalized wake velocity in the vertical plane through the rotation axis of the wind turbine in three different surging amplitudes and surging periods at state 2 (times of wind turbine passing the equilibrium position with negative additional velocity): (a) $A_s = 0.08$ m, $T_s = 4T$; (b) $A_s = 0.14$ m, $T_s = 4T$; (c) $A_s = 0.20$ m, $T_s = 4T$; (d) $A_s = 0.20$ m, $T_s = 8T$; (e) $A_s = 0.20$ m, $T_s = 2T$.

Therefore, the wake profiles in the far-wake region show the larger discrepancy.

For the wake profiles in different surging periods, Fig. 13 plots the wake profiles of the wind turbine in three surging periods of $T_s = 2T$, $4T$, and $8T$ at three downwind distances. In the near-wake region of $x = 1D$, the centerlines of the wake profile are the same in three different surging periods, but the velocity deficits near the centerline at these four stages are all increased with the decreasing surging periods. As shown in Fig. 14 (c)~(d), although the core region of the wake still locates at the center position of the blades in the vertical direction in these three cases, the velocity magnitudes show different values. This variation of the velocity deficit is mainly caused by the different values of V_{sa} and the disturbance frequency induced by the surge motion. The wake structures show noticeable differences from downwind distance $x = 3D$ under these surging periods in spite of the wind turbine being in the same motion state. When the wind turbine is located at the equilibrium position, the core strength of the 'Spindle' is improved in the lower surging period. Moreover, the positions of the 'Spindle' in these three cases are also different. In the condition of lower surging period, the wake structure in the far-wake region shows a more dispersed state and the core zone of the wake is scattered by a more violent disturbance. The disparate change of wake structures in the far-wake region leads to the diversity of the wake profile in different surging periods as shown in Fig. 13.

6. Conclusions

The CFD method with the IDDES model and the overset mesh technique are used in this paper to investigate the wake characteristics of an H-rotor wind turbine in a platform's pitch and surge motion. Wake profiles at several downwind distances from $1D$ to $11D$ and wake structures between pitch and non-pitch conditions are compared. It is shown that pitching motion can significantly alter the wake profiles of the wind turbine, and the degree of these changes is increasingly obvious in further downwind distances. The wake deficit can be increased in some states of pitch motion. The wake profiles under different pitching amplitudes and periods randomly change in the far wake region due to the fact that both the periods and amplitudes of the 'wake wave' change against the pitching amplitudes and periods.

The surge motion can also sharply change the wake profiles of the wind turbine because a 'Spindle' -type wake structure appears in the wake region and moves from the near-wake region to the far-wake region during one surging period. The strength of the 'Spindle' increases with the decrease of the surging periods, and the area of the 'Spindle' increases with the increase of the surging amplitudes. Further, the core zones of the wake structures that become more dispersive at the lower T_s and higher A_s have great influence on the wake profiles.

These findings in the present study may help to understand the wake characteristics of the H-rotor wind turbine in pitch and surge motion and can remind us that the impacts of the platform motion on wake modeling should be emphasized. A new challenging work of exploring wake modeling under the platform's motion is faced in the future.

Acknowledgements

The financial supports from the National Natural Science Foundation of China (Nos. 51879160, 11772193 and 51679139), Innovation Program of Shanghai Municipal Education Commission, the Shanghai Pujiang Program (No. 17PJ1404300), Shanghai Natural Science Foundation (Nos. 17ZR1415100 and 18ZR1418000), Project of Thousand Youth Talents(No. BE0100002) are gratefully acknowledged. This research is also sponsored in part by Program for Professor of Special Appointment (Eastern Scholar) at Shanghai Institutions of Higher Learning (No. ZXDF010037), Program for Intergovernmental International S&T Cooperation Projects of Shanghai Municipality (No. 18290710600) and New Enrolment Support of Shanghai Jiao Tong University (No. WF220401005). Hang Lei will acknowledge support from the China Scholarship Council.

References

[1] Song D, Yang J, Fan X, Liu Y, Liu A, Chen G, et al. Maximum power extraction for wind turbines through a novel yaw control solution using predicted wind directions. Energy Convers Manag 2018;157:587–99.
[2] Keivanpour S, Ramudhin A, Kadi DA. The sustainable worldwide offshore wind energy potential : a systematic review. J Renew Sustain Energy 2017;9. https://doi.org/10.1063/1.5009948.
[3] Byrne R, Hewitt NJ, Grif P, Macartain P. Observed site obstacle impacts on the energy performance of a large scale urban wind turbine using an electrical energy rose. Energy Sustain Dev 2018;43:23–37. https://doi.org/10.1016/j.esd.2017.12.002.
[4] Tran TT, Kim DH. A CFD study into the influence of unsteady aerodynamic interference on wind turbine surge motion. Renew Energy 2016;90:204–28.
[5] Song D, Yang J, Dong M, Joo YH. Model predictive control with finite control set for variable-speed wind turbines. Energy 2017;126:564–72.
[6] Breton SP, Moe G. Status, plans and technologies for offshore wind turbines in Europe and North America. Renew Energy 2009;34:646–54.
[7] Borg M, Shires A, Collu M. Offshore floating vertical axis wind turbines, dynamics modelling state of the art. part {I}: Aerodynamics. Renew Sustain Energy Rev 2014;39:1214–25.
[8] Borg M, Collu M, Kolios A. Offshore floating vertical axis wind turbines, dynamics modelling state of the art. Part {II}: mooring line and structural dynamics. Renew Sustain Energy Rev 2014;39:1214–25.
[9] Borg M, Collu M. Offshore floating vertical axis wind turbines, dynamics modelling state of the art. Part {III}: hydrodynamics and coupled modelling approaches. Renew Sustain Energy Rev 2015;46:296–310.
[10] Sebastian T, Lackner MA. Characterization of the unsteady aerodynamics of offshore floating wind turbines. Wind Energy 2013:339–52. https://doi.org/10.1002/we.
[11] Lin L, Wang K, Vassalos D. Detecting wake performance of floating offshore wind turbine. Ocean Eng 2018;156:263–76. https://doi.org/10.1016/j.oceaneng.2018.03.028.
[12] Á MI, Ting DS, Fartaj A. Aerodynamic models for Darrieus-type straight-bladed vertical axis wind turbines. Renew Sustain Energy Rev 2008;12:1087–109. https://doi.org/10.1016/j.rser.2006.10.023.
[13] Ghasemian M, Ashrafi ZN, Sedaghat A. A review on computational fluid dynamic simulation techniques for Darrieus vertical axis wind turbines. Energy Convers Manag 2017;149:87–100. https://doi.org/10.1016/j.enconman.2017.07.016.
[14] Elkhoury M, Kiwata T, Aoun E. Experimental and numerical investigation of a three-dimensional vertical-axis wind turbine with variable-pitch. J Wind Eng Ind Aerodyn 2015;139:111–23. https://doi.org/10.1016/j.jweia.2015.01.004.
[15] Buchner A-J, Lohry MW, Martinelli L, Soria J, Smits AJ. Dynamic stall in vertical axis wind turbines: comparing experiments and computations. J Wind Eng Ind Aerodyn 2015;146:163–71. https://doi.org/10.1016/j.jweia.2015.09.001.
[16] Lei H, Zhou D, Bao Y, Li Y, Han Z. Three-dimensional improved delayed detached eddy simulation of a two-bladed vertical axis wind turbine. Energy Convers Manag 2017;133:235–48. https://doi.org/10.1016/j.enconman.2016.11.067.
[17] Koo E, Jin EK, Linn R, Esparza DM. Large-eddy simulations of wind-farm wake characteristics associated with a low-level jet. 2018. p. 163–73. https://doi.org/10.1002/we.2152.
[18] Zuo W, Wang X, Kang S. Numerical simulations on the wake effect of H-type vertical axis wind turbines. Energy 2016;106:691–700.
[19] Frandsen S. Turbulence and turbulence- generated structural loading in wind turbine clusters, vol. 1188; 2007.
[20] Bianchini A, Balduzzi F, Ferrara G, Ferrari L, Persico G, Dossena V, et al. Detailed analysis of the wake structure of a straight-blade H-Darrieus wind turbine by means of wind tunnel experiments and CFD simulations. In: ASME Turbo Expo 2017 Turbomach. Tech. Conf. Expo.; 2017. V009T49A018–V009T49A018.
[21] Posa A, Parker CM, Leftwich MC, Balaras E. Wake structure of a single vertical axis wind turbine. Int J Heat Fluid Flow 2016:75–84.
[22] Bussel GJW Van, Tescione G, Sim CJ. Analysis of a free vortex wake model for the study of the rotor and near wake fl ow of a vertical axis wind turbine. Renew Energy 2016;87:552–63. https://doi.org/10.1016/j.renene.2015.10.002.
[23] Lam HF, Peng HY. Study of wake characteristics of a vertical axis wind turbine by two- and three-dimensional computational fluid dynamics simulations. Renew Energy 2016;90:386–98. https://doi.org/10.1016/j.renene.2016.01.011.
[24] Shamsoddin S, Porté-agel F. A large-eddy simulation study of vertical Axis wind turbine wakes in the atmospheric boundary layer. 2016. p. 1–23.

https://doi.org/10.3390/en9050366.
[25] Peng HY, Lam HF. Turbulence effects on the wake characteristics and aerodynamic performance of a straight-bladed vertical axis wind turbine by wind tunnel tests and large eddy simulations. Energy 2016;109:557–68. https://doi.org/10.1016/j.energy.2016.04.100.
[26] Abkar M, JO Dabiri, Abkar M, JO Dabiri. Self-similarity and flow characteristics of vertical- axis wind turbine wakes : an LES study. J Turbul 2017;18:373–89. https://doi.org/10.1080/14685248.2017.1284327.
[27] Lei H, Zhou D, Lu J, Chen C, Han Z, Bao Y. The impact of pitch motion of a platform on the aerodynamic performance of a floating vertical axis wind turbine. Energy 2017;119:369–83. https://doi.org/10.1016/j.energy.2016.12.086.
[28] Lei H, Zhou D, Bao Y, Chen C, Ma N, Han Z. Numerical simulations of the unsteady aerodynamics of a fl oating vertical axis wind turbine in surge motion. Energy 2017;127:1–17. https://doi.org/10.1016/j.energy.2017.03.087.
[29] Tran TT, Dong HK. The aerodynamic interference effects of a floating offshore wind turbine experiencing platform pitching and yawing motions. J Mech Sci Technol 2015;29:549–61.
[30] Bayo R, Rockel S, Peinke J, Michael H. Dynamic wake development of a floating wind turbine in free pitch motion subjected to turbulent inflow generated with an active grid, vol. 112; 2017. p. 1–16. https://doi.org/10.1016/j.renene.2017.05.016.
[31] Rockel S, Camp E, Schmidt J, Peinke J. Experimental study on influence of pitch motion on the wake of a floating wind turbine model '. 2014. https://doi.org/10.3390/en7041954.
[32] Dörenkämper M, Witha B, Steinfeld G, Heinemann D, Kühn M. The impact of stable atmospheric boundary layers on wind-turbine wakes within offshore wind farms, vol. 144; 2015. p. 146–53. https://doi.org/10.1016/j.jweia.2014.12.011.
[33] Bayati I. Wind tunnel wake measurements of floating offshore wind turbines measurements measurements. Energy Procedia 2017;137:214–22. https://doi.org/10.1016/j.egypro.2017.10.375.
[34] Nematbakhsh A, Bachynski EE, Gao Z, Moan T. Comparison of wave load effects on a TLP wind turbine by using computational fluid dynamics and potential flow theory approaches. Appl Ocean Res 2015;53:142–54.
[35] Tran T-T, Kim D-H. The platform pitching motion of floating offshore wind turbine: a preliminary unsteady aerodynamic analysis. J Wind Eng Ind Aerodyn 2015;142:65–81.
[36] Li Q, Maeda T, Kamada Y, Murata J, Yamamoto M, Ogasawara T, et al. Study on power performance for straight-bladed vertical axis wind turbine by field and wind tunnel test. Renew Energy 2016;90:291–300. https://doi.org/10.1016/j.renene.2016.01.002.
[37] Li Q, Maeda T, Kamada Y, Ogasawara T, Nakai A. Investigation of power performance and wake on a straight-bladed vertical axis wind turbine with fi eld experiments. Energy 2017;141:1113–23. https://doi.org/10.1016/j.energy.2017.10.009.
[38] Subramanian A, Yogesh SA, Sivanandan H, Giri A, Vasudevan M, Mugundhan V, et al. Effect of airfoil and solidity on performance of small scale vertical axis wind turbine using three dimensional CFD model. Energy 2017;133:179–90. https://doi.org/10.1016/j.energy.2017.05.118.
[39] Tominaga Y, Stathopoulos T. Journal of Wind Engineering CFD modeling of pollution dispersion in a street canyon : comparison between LES and RANS. J Wind Eng Ind Aerodyn 2011;99:340–8. https://doi.org/10.1016/j.jweia.2010.12.005.
[40] Shur ML, Spalart PR, Strelets MK, Travin AK. A hybrid RANS-LES approach with delayed-DES and wall-modelled LES capabilities. Int J Heat Fluid Flow 2008;29:1638–49.
[41] CD-adapco U. GUIDE: STAR-CCM+ 2009.
[42] Larose GL, D'Auteuil A, Larose GL, D'Auteuil A. Effect of local air compressibility on the aerodynamics of rectangular prisms at Mach number below 0.3. 6th Int Colloq Bluff Body Aerodyn from 7/20/2008 to 7/24/2008 n.d.
[43] Demirdžić I, Muzaferija S. Numerical method for coupled fluid flow, heat transfer and stress analysis using unstructured moving meshes with cells of arbitrary topology. Comput Methods Appl Mech Eng 1995;125:235–55.
[44] Cai X, Gu R, Pan P, Zhu J. Unsteady aerodynamics simulation of a full-scale horizontal axis wind turbine using CFD methodology. Energy Convers Manag 2016;112:146–56.
[45] Collu M, Borg M, Rizzo NF, Lupi E. FloVAWT: further progresses on the development of a coupled model of dynamics for floating offshore VAWTS. In: Int. Conf. Ocean. Offshore Arct. Eng.; 2014. V09BT09A044.
[46] Lei H, Zhou D, Lu J, Chen C, Han Z, Bao Y. The impact of pitch motion of a platform on the aerodynamic performance of a fl oating vertical axis wind turbine. Energy 2017;119:369–83. https://doi.org/10.1016/j.energy.2016.12.086.